Research Article | Vol. 9, No. 2 | 1 Feb 2018 | BIOMEDICAL OPTICS EXPRESS 603
Biomedical Optics EXPRESS

Plasmonic nanoparticle-based expansion microscopy with surface-enhanced Raman and dark-field spectroscopic imaging

CAMILLE G. ARTUR,[1] TASHA WOMACK,[2] FUSHENG ZHAO,[1] JASON L. ERIKSEN,[2] DAVID MAYERICH,[1] AND WEI-CHUAN SHIH [1,3,4,5,*]

[1]*Department of Electrical and Computer Engineering, University of Houston, 4800 Calhoun Rd., Houston, TX 77004, USA*
[2]*Department of Pharmacological and Pharmaceutical Sciences, University of Houston College of Pharmacy, Houston, TX 77004, USA*
[3]*Department of Biomedical Engineering, University of Houston, 4800 Calhoun Rd, Houston, TX 77004, USA*
[4]*Program of Materials Science and Engineering, University of Houston, 4800 Calhoun Rd., Houston, TX 77004, USA*
[5]*Department of Chemistry, University of Houston, 4800 Calhoun Rd., Houston, TX 77004, USA*
[*]*wshih@central.uh.edu*

Abstract: Fluorescence-based expansion microscopy (ExM) is a new technique which can yield nanoscale resolution of biological specimen on a conventional fluorescence microscope through physical sample expansion up to 20 times its original dimensions while preserving structural information. It however inherits known issues of fluorescence microscopy such as photostability and multiplexing capabilities, as well as an ExM-specific issue in signal intensity reduction due to a dilution effect after expansion. To address these issues, we propose using antigen-targeting plasmonic nanoparticle labels which can be imaged using surface-enhanced Raman scattering spectroscopy (SERS) and dark-field spectroscopy. We demonstrate that the nanoparticles enable multimodal imaging: bright-field, dark-field and SERS, with excellent photostability, contrast enhancement and brightness.

OCIS codes: (170.3880) Medical and biological imaging; (180.5655) Raman microscopy; (170.5660) Raman spectroscopy; (240.6680) Surface plasmons; (240.6695) Surface-enhanced Raman scattering; (170.6510) Spectroscopy, tissue diagnostics; (170.6935) Tissue characterization.

References and links

1. S. W. Hell and J. Wichmann, "Breaking the diffraction resolution limit by stimulated emission: stimulated-emission-depletion fluorescence microscopy," Opt. Lett. **19**, 780–782 (1994).
2. E. Betzig, G. H. Patterson, R. Sougrat, O. W. Lindwasser, S. Olenych, J. S. Bonifacino, M. W. Davidson, J. Lippincott-Schwartz, and H. F. Hess, "Imaging intracellular fluorescent proteins at nanometer resolution," Science **313**, 1642–1645 (2006).
3. M. J. Rust, M. Bates, and X. Zhuang, "Sub-diffraction-limit imaging by stochastic optical reconstruction microscopy (STORM)." Nat. Methods **3**, 793–795 (2006).
4. F. Chen, P. W. Tillberg, and E. S. Boyden, "Expansion microscopy," Science **347**, 543–548 (2015).
5. T. Ku, J. Swaney, J.-Y. Park, A. Albanese, E. Murray, J. H. Cho, Y.-G. Park, V. Mangena, J. Chen, and K. Chung, "Multiplexed and scalable super-resolution imaging of three-dimensional protein localization in size-adjustable tissues." Nat. Biotechnol. **34**, 973–981 (2016).
6. P. W. Tillberg, F. Chen, K. D. Piatkevich, Y. Zhao, C.-C. J. Yu, B. P. English, L. Gao, A. Martorell, H.-J. Suk, F. Yoshida, E. M. DeGennaro, D. H. Roossien, G. Gong, U. Seneviratne, S. R. Tannenbaum, R. Desimone, D. Cai, and E. S. Boyden, "Protein-retention expansion microscopy of cells and tissues labeled using standard fluorescent proteins and antibodies," Nat. Biotechnol. **34**, 987–992 (2016).
7. J.-B. Chang, F. Chen, Y.-G. Yoon, E. E. Jung, H. Babcock, J. S. Kang, S. Asano, H.-J. Suk, N. Pak, P. W. Tillberg, A. T. Wassie, D. Cai, and E. S. Boyden, "Iterative expansion microscopy," Nat. Methods **14**, 593–599 (2017).
8. Y. Zhao, O. Bucur, H. Irshad, F. Chen, A. Weins, A. L. Stancu, E.-Y. Oh, M. DiStasio, V. Torous, B. Glass, I. E. Stillman, S. J. Schnitt, A. H. Beck, and E. S. Boyden, "Nanoscale imaging of clinical specimens using pathology-optimized

#305455 https://doi.org/10.1364/BOE.9.000603
Journal © 2018 Received 5 Sep 2017; revised 4 Jan 2018; accepted 4 Jan 2018; published 12 Jan 2018

Biomedical Optics EXPRESS

expansion microscopy." Nat. Biotechnol. (2017).
9. L. Wei, Z. Chen, L. Shi, R. Long, A. V. Anzalone, L. Zhang, F. Hu, R. Yuste, V. W. Cornish, and W. Min, "Super-multiplex vibrational imaging," Nature **544**, 465–470 (2017).
10. C. W. Freudiger, W. Min, B. G. Saar, S. Lu, G. R. Holtom, C. He, J. C. Tsai, J. X. Kang, and X. S. Xie, "Label-free biomedical imaging with high sensitivity by stimulated Raman scattering microscopy," Science **322**, 1857–1861 (2008).
11. C. M. MacLaughlin, N. Mullaithilaga, G. Yang, S. Y. Ip, C. Wang, and G. C. Walker, "Surface-enhanced Raman scattering dye-labeled Au nanoparticles for triplexed detection of leukemia and lymphoma cells and SERS flow cytometry," Langmuir **29**, 1908–1919 (2013).
12. J.-H. Kim, J.-S. Kim, H. Choi, S.-M. Lee, B.-H. Jun, K.-N. Yu, E. Kuk, Y.-K. Kim, D. H. Jeong, M.-H. Cho, and Y.-S. Lee, "Nanoparticle probes with surface enhanced Raman spectroscopic tags for cellular cancer targeting," Anal. Chem. **78**, 6967–6973 (2006).
13. B. Lutz, C. Dentinger, L. Sun, L. Nguyen, J. Zhang, A. Chmura, A. Allen, S. Chan, and B. Knudsen, "Raman nanoparticle probes for antibody-based protein detection in tissues," J. Histochem. Cytochem. **56**, 371–379 (2008).
14. S. Penn, R. Cromer, M. Sha, B. Doering, B. Brown, S. Norton, and I. Walton, "Nanoplex® biotags: Near-IR excited, highly multiplexed nanoparticulate optical detection tags for diagnostic assays" http://nsti.org/publications/Nanotech/2007/pdf/741.pdf.
15. M. Salehi, L. Schneider, P. Ströbel, A. Marx, J. Packeisen, and S. Schlücker, "Two-color SERS microscopy for protein co-localization in prostate tissue with primary antibody–protein A/G –gold nanocluster conjugates," Nanoscale **6**, 2361–2367 (2014).
16. L. Fabris, "Gold-based SERS tags for biomedical imaging," J. Opt. **17**, 114002 (2015).
17. Y. Wang, B. Yan, and L. Chen, "SERS tags: novel optical nanoprobes for bioanalysis," Chem. Rev. **113**, 1391–1428 (2012).
18. E. Le Ru, E. Blackie, M. Meyer, and P. G. Etchegoin, "Surface enhanced Raman scattering enhancement factors: a comprehensive study," J. Phys. Chem. C **111**, 13794–13803 (2007).
19. A. Pallaoro, G. B. Braun, and M. Moskovits, "Biotags based on surface-enhanced Raman can be as bright as fluorescence tags," Nano Lett. **15**, 6745–6750 (2015).
20. J. Qi and W.-C. Shih, "Performance of line-scan Raman microscopy for high-throughput chemical imaging of cell population," Appl. Opt. **53**, 2881–2885 (2014).
21. N. Sudheendran, J. Qi, E. D. Young, A. J. Lazar, D. C. Lev, R. E. Pollock, K. V. Larin, and W.-C. Shih, "Line-scan Raman microscopy complements optical coherence tomography for tumor boundary detection," Laser Phys. Lett. **11**, 105602 (2014).
22. S. Schlücker, M. D. Schaeberle, S. W. Huffman, and I. W. Levin, "Raman microspectroscopy: a comparison of point, line, and wide-field imaging methodologies," Anal. Chem. **75**, 4312–4318 (2003).
23. R. J. Mullen, C. R. Buck, and A. M. Smith, "NeuN, a neuronal specific nuclear protein in vertebrates," Development **116**, 201–211 (1992).
24. D. Lind, S. Franken, J. Kappler, J. Jankowski, and K. Schilling, "Characterization of the neuronal marker NeuN as a multiply phosphorylated antigen with discrete subcellular localization," J. Neurosci. Res. **79**, 295–302 (2005).
25. A. M. Lavezzi, M. F. Corna, and L. Matturri, "Neuronal nuclear antigen (NeuN): a useful marker of neuronal immaturity in sudden unexplained perinatal death," J. Neurol. Sci. **329**, 45–50 (2013).
26. S. Schlücker, B. Küstner, A. Punge, R. Bonfig, A. Marx, and P. Ströbel, "Immuno-Raman microspectroscopy: in situ detection of antigens in tissue specimens by surface-enhanced Raman scattering," J. Raman Spectrosc. **37**, 719–721 (2006).
27. A. Indrasekara, B. J. Paladini, D. J. Naczynski, V. Starovoytov, P. V. Moghe, and L. Fabris, "Dimeric gold nanoparticle assemblies as tags for SERS-based cancer detection," Adv. Healthcare Mater. **2**, 1370–1376 (2013).
28. W. L. Barnes, A. Dereux, and T. W. Ebbesen, "Surface plasmon subwavelength optics," Nature **424**, 824 (2003).
29. G. W. Bryant, F. J. García de Abajo, and J. Aizpurua, "Mapping the plasmon resonances of metallic nanoantennas," Nano Lett. **8**, 631–636 (2008).
30. J. N. Anker, W. P. Hall, O. Lyandres, N. C. Shah, J. Zhao, and R. P. Van Duyne, "Biosensing with plasmonic nanosensors," Nat. Mater. **7**, 442–453 (2008).
31. K. A. Willets and R. P. Van Duyne, "Localized surface plasmon resonance spectroscopy and sensing," Annu. Rev. Phys. Chem. **58**, 267–297 (2007).
32. J. Chen, F. Saeki, B. J. Wiley, H. Cang, M. J. Cobb, Z.-Y. Li, L. Au, H. Zhang, M. B. Kimmey, Li, and Y. Xia, "Gold nanocages: bioconjugation and their potential use as optical imaging contrast agents," Nano Lett. **5**, 473–477 (2005).
33. K. Sokolov, M. Follen, J. Aaron, I. Pavlova, A. Malpica, R. Lotan, and R. Richards-Kortum, "Real-time vital optical imaging of precancer using anti-epidermal growth factor receptor antibodies conjugated to gold nanoparticles," Cancer Res. **63**, 1999–2004 (2003).
34. I. H. El-Sayed, X. Huang, and M. A. El-Sayed, "Surface plasmon resonance scattering and absorption of anti-EGFR antibody conjugated gold nanoparticles in cancer diagnostics: applications in oral cancer," Nano Lett. **5**, 829–834 (2005).
35. C. Yu, H. Nakshatri, and J. Irudayaraj, "Identity profiling of cell surface markers by multiplex gold nanorod probes," Nano Lett. **7**, 2300–2306 (2007).
36. L. Tong, Q. Wei, A. Wei, and J.-X. Cheng, "Gold nanorods as contrast agents for biological imaging: optical

Biomedical Optics EXPRESS

properties, surface conjugation and photothermal effects," Photochem. Photobiol. **85**, 21–32 (2009).
37. F. Zhao, M. M. P. Arnob, O. Zenasni, J. Li, and W.-C. Shih, "Far-field plasmonic coupling in 2-dimensional polycrystalline plasmonic arrays enables wide tunability with low-cost nanofabrication," Nanoscale Horiz. (2017).
38. C.-F. Chen, S.-D. Tzeng, H.-Y. Chen, K.-J. Lin, and S. Gwo, "Tunable plasmonic response from alkanethiolate-stabilized gold nanoparticle superlattices: evidence of near-field coupling," J. Am. Chem. Soc. **130**, 824–826 (2008).
39. P. K. Jain and M. A. El-Sayed, "Plasmonic coupling in noble metal nanostructures," Chem. Phys. Lett. **487**, 153 – 164 (2010).
40. J. Zuloaga and P. Nordlander, "On the energy shift between near-field and far-field peak intensities in localized plasmon systems," Nano Lett. **11**, 1280–1283 (2011).
41. P. K. Jain, K. S. Lee, I. H. El-Sayed, and M. A. El-Sayed, "Calculated absorption and scattering properties of gold nanoparticles of different size, shape, and composition: applications in biological imaging and biomedicine," J. Phys. Chem. B **110**, 7238–7248 (2006).
42. M. M. P. Arnob, F. Zhao, J. Li, and W.-C. Shih, "Ebl-based fabrication and different modeling approaches for nanoporous gold nanodisks," ACS Photonics **4**, 1870–1878 (2017).
43. K. Faulds, R. Jarvis, W. E. Smith, D. Graham, and R. Goodacre, "Multiplexed detection of six labelled oligonucleotides using surface enhanced resonance Raman scattering (SERRS)," Analyst **133**, 1505–1512 (2008).
44. G. von Maltzahn, A. Centrone, J.-H. Park, R. Ramanathan, M. J. Sailor, T. A. Hatton, and S. N. Bhatia, "SERS-coded gold nanorods as a multifunctional platform for densely multiplexed near-infrared imaging and photothermal heating," Adv. Mater. **21**, 3175–3180 (2009).
45. X. Wei, S. Su, Y. Guo, X. Jiang, Y. Zhong, Y. Su, C. Fan, S.-T. Lee, and Y. He, "A molecular beacon-based signal-off surface-enhanced Raman scattering strategy for highly sensitive, reproducible, and multiplexed dna detection," Small **9**, 2493–2499 (2013).
46. J. Qi, J. Zeng, F. Zhao, S. H. Lin, B. Raja, U. Strych, R. C. Willson, and W.-C. Shih, "Label-free, in situ SERS monitoring of individual DNA hybridization in microfluidics," Nanoscale **6**, 8521–8526 (2014).

1. Introduction

Molecular labeling plays a crucial role in biomedical imaging, including microbiology, histopathology, and disease diagnosis. The most common techniques include immunohistochemistry and immunofluorescence, which can be used to visualize the distribution of highly specific molecules. However, these methods provide spatial resolution limited by the point spread function of the imaging system, and fundamentally by the diffraction limit of light. Recent advances in super-resolution (SR) imaging, including stimulated emission/depletion (STED) microscopy [1], photoactivated localization microscopy (PALM) [2], and stochastic optical reconstruction microscopy (STORM) [3], break the diffraction limit by either point-spread function engineering or single molecule fluorescence localization. However, these SR methods face similar limitations in spectral real-estate as other fluorescence-based techniques, since they rely on emission in the narrow visible range.

A recent alternative is expansion microscopy (ExM) [4–7], which circumvents the optical challenge by embedding the sample within a swellable polymer matrix that expands isotropically, allowing spatial features below the diffraction limit to become resolvable with non-SR imaging systems. While studies using this technique have been tested on a variety of tissue types [8], they however inherit known issues of fluorescence microscopy such as photostability and multiplexing capabilities. In addition, the expansion process significantly dilutes label concentrations, resulting in diminishing signal to noise ratio. Further, ExM requires a digestion step that cleaves proteins to allow for expansion. While the effect of this step on target epitopes is not well understood, performing multi-pass multiplex labeling may be impractical.

Recent research suggests that large-scale (24+) multiplex imaging is possible with functionalized near-infrared dyes [9] with a stimulated Raman scattering (SRS) set-up [10]. This technique takes advantage of the much narrower linewidths ($\approx$1 nm) of Raman spectral bands compared to fluorescent bands which can be as wide as 50 nm. However, a SRS imaging system typically involves two ultrafast laser pulses, frequency modulation, and lock-in detection, which represent significant technical and resource barriers. Alternatively, this signal can be amplified using surface-enhanced Raman scattering (SERS) nanotags. These tags are antibody-conjugated

Biomedical Optics EXPRESS

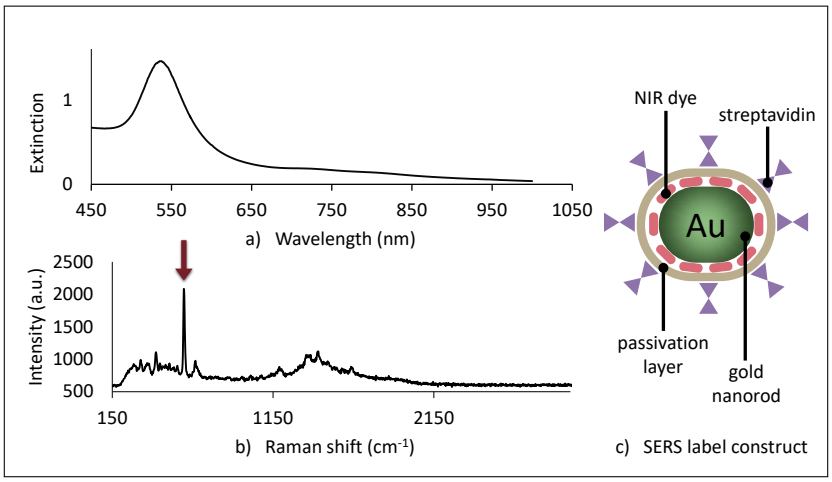

Fig. 1. UV-visible extinction spectrum (a) (Hitachi UV-vis spectrophotometer U-2001) and SERS spectrum (b) of the construct as received, diluted 20 times in PBS 1X (Sigma), which corresponds to an approximate concentration of 6.10^{12} nanoparticles per mL (c) Streptavidin conjugated NPs markers for immuno-labeling. SERS measurements were obtained with 785 nm line excitation, 60 mW total power at the sample plane and 1 s integration. The SERS spectrum of the label A features a sharp and intense characteristic mode at 590 cm^{-1} (red arrow on b).

SERS active metallic nanoparticles (NPs) functionalized with a Raman reporter [11–17]. Such nanostructures produce strong characteristic SERS signals and allow imaging of targeted antigens via a Raman microscope. These constructs harness the localized surface plasmon resonances (LSPR) of the underlying Au NPs to enhance the characteristic Raman signal of the adsorbed dye by several orders of magnitude [18].These tags can be engineered to be at least as bright as conventional fluorescent organic biomarkers [19] with increased photostability at resonance compared to organic fluorescent emitters and using NPs tags naturally enables an additional imaging modality via dark-field spectroscopy.

In this paper, we propose the use of commercially available gold nanoparticles that are functionalized for antigen binding and labeled with distinct near-infrared (NIR) Raman dyes that are protected from the environment by a passivation layer. We demonstrate that these NPs are effective for histological labeling in standard fixed paraffin-embedded (FPE) tissue sections and have several features that make them well suited for ExM, namely increased photostability, high dark-field contrast and sensitivity to binding sites separation distances through plasmonic coupling effects.

2. Materials and methods

2.1. Nanoparticle labels

Conjugated NPs (Nanopartz Ramanprobes™, Nanopartz Inc.) were purchased and used for histological labeling. These probes are highly monodisperse SERS active gold nanoparticles 10 nm in diameter and 13 nm in length, labeled with a monolayer of NIR Raman active dye (hereafter named “label A”). The construct is protected from chemically interacting with the environment by a pH and salt resistant polymer layer onto which an average of 9 streptavidin molecules are covalently attached (Fig. 1).

The gold nanoparticles have a LSPR peak at 540 nm in water, the colloidal solution is very stable, and the optical response is very close to the orientation averaged response of a single

Biomedical Optics EXPRESS

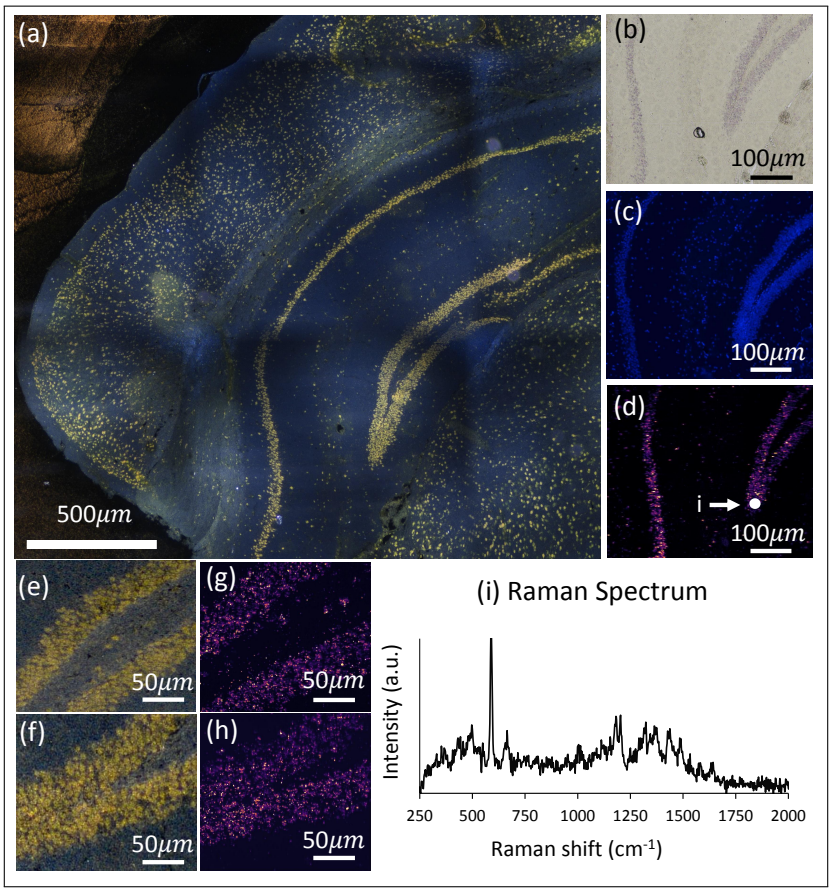

Fig. 2. Validation pre-expansion of the SERS nanoparticles labeling of NeuN in mouse brain coronal 10 μm sections. a) Dark-field mosaic microphotograph. Bright-field (b), DAPI (c) and SERS (d) detail of the dentate gyrus granule cell layer and pyramidal layer. Close-up dark-field (e,f) photographs and corresponding SERS (g,h) maps of the densely packed granule cells with larger pyramidal cells in between. Raw SERS spectrum (i) collected from the circled area in (d). The SERS images are mapping the total integrated intensity of the 590 cm^{-1} peak. SERS spectras acquisition 1 s, 60 mW total power incident at the sample plane.

nanorod. The representative SERS spectrum of label A (Fig. 1(a)) shows a strong mode at 590 cm^{-1}. The signal is bright and there is no fluorescence background. The spectral sharpness of Raman bands and their molecular specificity make these labels ideal candidates for multiplexing studies.

2.2. Tissue preparation

Wild type (wt) mouse Accustain (Sigma) fixed paraffin embedded 10 μm mouse brain coronal sections were cut and placed on charged glass slides, deparaffinized (xylene substitute, Sigma) and progressively re-hydrated. The tissue sections were blocked for 5 minutes with IncrediBlock Advance Free (Teomics) serum-free block to reduce unspecific binding. The sections were then rinsed twice with PBS 1X (Phosphate buffered saline reconstituted in deionized water from powdered form, Sigma). The sections were stained with the primary monoclonal MAB377 Anti-NeuN antibody clone A60 from EMD Millipore diluted 1:500 in PBS for an hour at room

Biomedical Optics EXPRESS

temperature while negative control sections were incubated in PBS. After two rinses in PBS, the sections were incubated in the biotinylated antiPoly secondary antibody (Teomics) for 10 minutes at room temperature and rinsed twice in PBS. Sections were incubated with the NPs labels diluted 1:20 (10^{12} nanoparticles per mL) in PBS for one hour at room temperature. The slices were finally rinsed thoroughly in PBS. Sections destined for imaging pre-expansion were mounted in Fluorogel II plus DAPI (Electron Microscope Sciences) and cover-slipped.

2.3. Tissue expansion

Expansion of the stained brain sections was performed following a previously published protocol [6]. Briefly, the protein anchoring treatment was prepared by re-suspending Acryloyl X-SE (AcX, Fisher) in 500 μL anhydrous dimethyl sulfoxide (DMSO, Sigma) to reach a stock concentration of 0.1 mg/mL. The NPs-labeled brain sections were incubated overnight at room temperature in AcX diluted 1:100 in PBS. The sections were then washed twice in PBS for 15 minutes per rinse.

Aliquots of 9.4 mL of monomer solution were prepared by mixing the following: 2.25 mL sodium acrylate (concentration 38 g/100 mL, Sigma), 0.5 mL acrylamide (concentration 50 g/100 mL, Sigma), 0.75 mL N,N'-methylbisacrylamide (concentration 2 g/100 mL, Sigma), 4 mL sodium chloride (concentration 29.2 g/100 mL, Fisher), 1 mL PBS 10X and 0.9 mL deionized water. A gelling chamber was then designed around each section on glass by enclosing the tissue into a 6.8 mm diameter and 1 mm depth polydimethylsiloxane (PDMS) well. After removal of the excess PBS, the sections were incubated in the monomer solution for an hour at 4 °C to allow for the diffusion of the monomers throughout the tissue. The gelling solution (200 μL) was then prepared on ice by adding in the following order: 188 μL monomer solution, 4 μL of 4-hydroxy-TEMPO (Sigma) 0.5% (inhibits premature gelation), 4 μL of tetramethylethylenediamine (TEMED, Sigma) 10% (accelerates the radical generation) and 4 μL of ammonium persulfate 10% (APS, Sigma, initiates radical production). After incubation into the monomer solution, excess monomer solution was removed from the wells and 50 μL of gelling solution was added onto each brain section. Gelling chambers were sealed by covering each well by a coverslip wrapped in parafilm. The samples were then incubated at 37 °C for an hour and half or until complete gelation. After gelation, coverglass and PDMS wells were removed. The gels were then incubated overnight at room temperature into a large excess volume of digestion solution consisting of Proteinase K 1:100 (New England Biolabs) in 50 mM tris pH 8.0, 1 mM EDTA, 0.5% triton X-100 and 0.8 M guanidine HCl (Sigma). After digestion, the gelled slices detached from the glass and became totally transparent. The gels were then washed twice in PBS for 15 min each then placed in deionized water to expand. The step was repeated four times until expansion stopped.

2.4. Traditional microscopy

Bright-field, dark-field, and fluorescence microphotographs were obtained on a Nikon Ti-E inverted fluorescent microscope equipped with an X-Cite 200 LED source for epi-fluorescence and a Nikon Ti-DF condenser for the acquisition of the dark-field mosaic pictures. Spectrally-resolved dark-field photographs were obtained on a home-built instrument consisting of an Olympus IX71 inverted microscope equipped with a dark-field condenser (Olympus DCW 1.4-1.2), an imaging spectrometer (Acton SP-2300i), and a CCD camera (Princeton instrument PIXIS 400). SERS spectra and hyperspectral maps were obtained on a home-built line-scan system consisting of an Olympus IX71 inverted microscope, an imaging spectrometer (Acton SP-2300i), and a CCD camera (Princeton instrument PIXIS 400). The 785 nm excitation source is the output of a tunable Titanium:Sapphire CW laser (Newport 3900S) with 3W maximum output.

Biomedical Optics EXPRESS

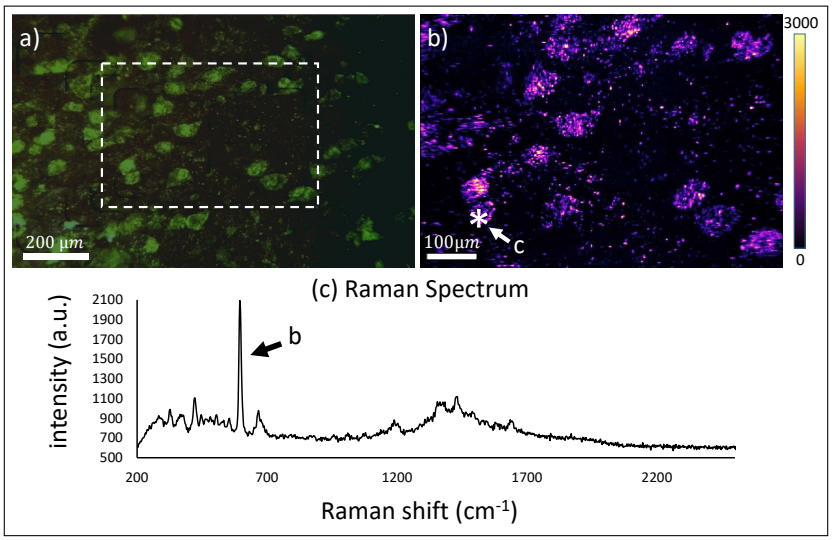

Fig. 3. Expansion of the brain sections stained for NeuN with the SERS nanoparticles. Dark-field (a) and SERS (590 cm^{-1} band) (b) images of the expanded isocortex. (c) SERS spectrum collected from the circled area, total incident power at the sample plane 630 mW, integration 0.5 s.

2.5. Hyperspectral SERS maps acquisition

SERS imaging was realized on a home-built line-scan Raman system [20, 21]. Line-scanning provides an improvement in imaging speed over point scanning in micro-Raman spectroscopy [22]. We take advantage of 2D CCD arrays to obtain simultaneous spatial and spectral information. The CCD detector consists of an array of 400×1340 pixels. The line is imaged along the 400-pixel dimension while the 1340-pixel dimension is used to resolve the wavelength-dispersed signal. The line is scanned along the sample plane using a gavanometric mirror, resulting in a hyperspectral datacube containing the Raman spectra for each (x,y) points of the scanned area. A 300 l/mm grating (blazed at 820 nm) is used with a entrance slit of 50 μm which yields a spectral resolution of ≈2.4 cm^{-1}.

3. Results

3.1. Validation of the NPs labeling pre-expansion

The NeuN protein is a neuronal nuclear antigen which is widely expressed in the nucleus and peri-nuclear cytoplasm of diverse post-mitotic neuronal cells; intense NeuN expression is expected in healthy neurons [23–25].The results of the staining pre-expansion of NeuN with the NPs labels in mouse brain sections of the hippocampal dentate gyrus are shown in Fig. 2. We found that immunostaining with the nanoparticles enables efficient multimodal imaging of the NeuN epitopes. As we will discuss hereafter, the intrinsic brightness of the labels adds on the amplification of the signal due to the indirect staining scheme, all the while having no other background signal than that of a minimal unspecific binding. Furthermore, the staining process outcome can be easily asserted on a bench-top white-light microscope as purple structures and under grazing light as red-gold structures.

Unlike traditional conjugated dyes used in immunofluorescence microscopy which require a special excitation/emission filter set, the proposed NPs labels are also visible in conventional bright-field and dark-field conditions. Due to the gold nanoparticle strong optical absorption at

Biomedical Optics EXPRESS

540 nm, the nanoparticle stained areas on the tissue appear purple under diascopic white light illumination (Fig. 2(b)). Scattering at the LSPR wavelength of the nanostructures is enhanced and confers dark-field images an intense and colorful contrast, as can be appreciated on Fig. 2(a), 2(e) and 2(f), making landmark stained structures very easy to locate. The SERS 2D images (Fig. 2(d), 2(g) and 2(h)) are produced from the intensity of the 590 cm^{-1} band of the label A covering the gold nanoparticles. Similar images - not shown here - can be obtained by mapping the intensity of several other sharp Raman-active modes of the label. The SERS spectra did not need any processing due to the absence of any fluorescence background beside the luminescence of the thick charged microscope slide onto which the brain sections are mounted and thus, the raw data are presented. The sharp and distinct SERS peaks indicate a good representation of the "fingerprinting" property of Raman spectroscopy, which is envisioned to provide better multiplexing capability in future studies with different SERS nanotags.

A relatively low incident laser power of 60 mW at 785 nm excitation is used for the maps presented in this section; the power is in effect distributed along the 750 μm×6μm (resp. 187.5 μm×4μm) focal line at the sample plane with a 10X, NA=0.3 (resp. 40X, NA=0.75) and acquisition time was 1 s per line-spectrum. Images were constructed by stepping the line for 200 steps which translates to a total acquisition time for a full datacube of approximately 200 s, a throughput that is higher than point-by-point SERS mapping of tissue previously reported [12, 15, 26, 27]. We would like to also point out that no loss of SERS signal was observed under higher laser power and longer illumination. It is hence possible to increase the incident power and further reduce the integration time. Furthermore, we also report here that tissue sections which were stained with the SERS labels and mounted in an aqueous mounting medium such as Fluorogel showed no detectable decrease in SERS intensity after several months stored under indoor ambient light.

3.2. Expansion of the NPs-labeled mouse brain section

After immuno-labeling of the NeuN epitopes on the mouse brain sections by the NPs, sections were expanded as described in section 2.3. The pre-treatment of the stained sections with Acryloyl X-SE (succinimidyl ester of (6-((acryloyl)amino)hexanoic acid), AcX) ensures that proteins, whether native to the tissue or label-conjugated antibodies, will be anchored to the polymer matrix [6] as AcX reacts with amines to yield acrylamides species that can be co-polymerized into polyacrylamide matrices.

Results of the expansion protocol using the NPs are presented in Fig. 3(a) and 3(b). The conjugated NPs labels underwent the expansion protocol and were successfully anchored to the gel matrix and preserved, validating their use as protease-resistant tags for ExM. Indeed, the penultimate step of the expansion protocol, digestion of the gel embedded sections by the proteinase K, prepares the samples for isotropic expansion through strong proteolytic homogenization. As Tillberg et al. discussed in the protein-retention ExM study [6], complete proteolytic digestion is required to yield reliable expansion; pre-treatment of the stained sections with AcX anchors and preserves the fluorescence of commercial dye conjugated secondary antibodies. We estimate the expansion factor to be ≈ 4.

The use of ExM resulted in a striking color shift of NPs structures, changing from red-yellow to green, in dark-field (Fig. 2 and 3). In bright-field, structures and tissue are no longer visible after expansion. Indeed, the strong proteolysis of the tissue has also an optical clearing effect; expanded gels are index-matched with water and autofluorescence from the original tissue is greatly reduced.

For the SERS mapping measurements (Fig. 3), the expanded gels were placed on a large microscope slide and imaged in back-scattering configuration with the a 10X NA=0.3 objective with 630 mW total incident power and 0.5 s integration per line (see Section 3.1).The 10X objective lens was employed to include a sufficiently large field of view without a scanning

Biomedical Optics EXPRESS

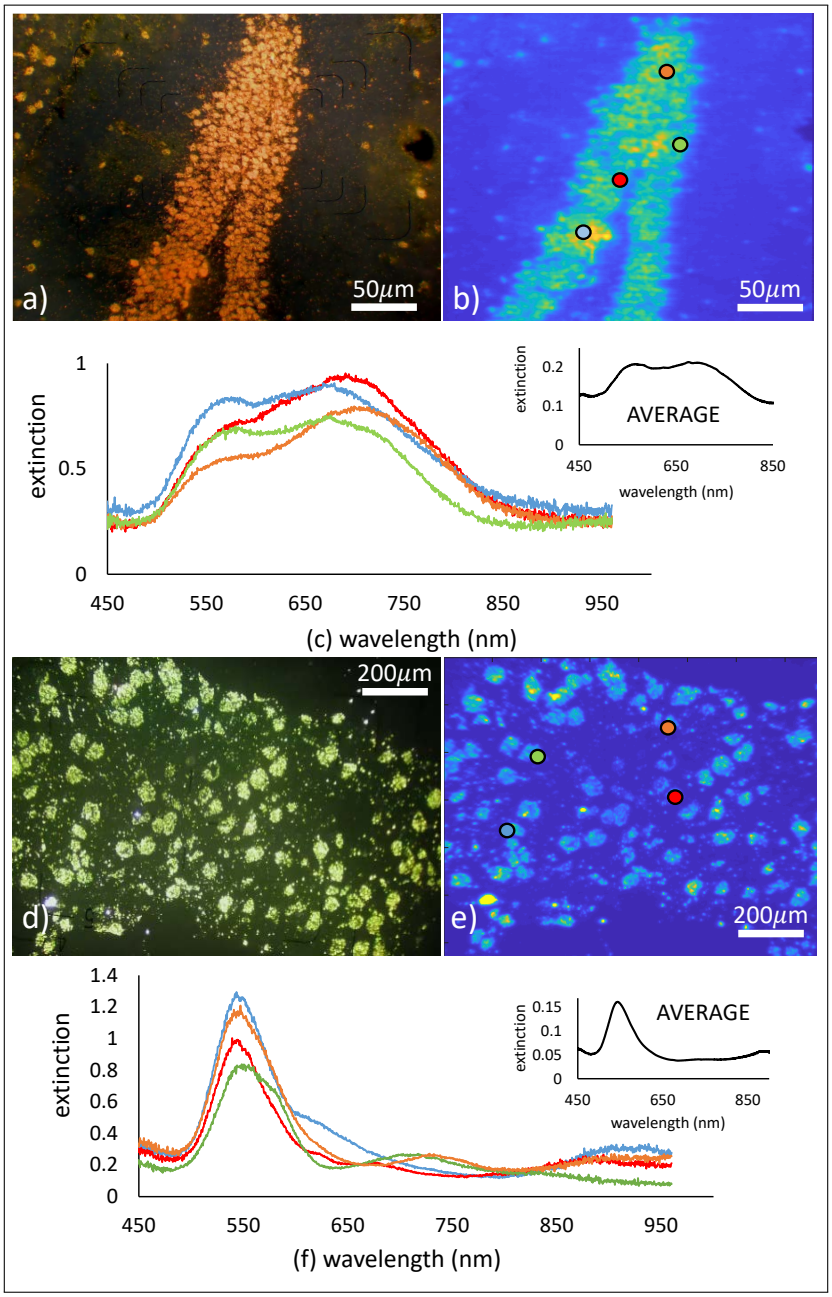

Fig. 4. Dark-field (a) and UV-vis total integrated extinction map (b) of the dentate gyrus pre-expansion. UV-vis extinction spectra (c) collected at the circled areas in (b) and average extinction spectrum over the whole image. Dark-field (d) and UV-vis total integrated extinction map (e) of neurons in the cerebral cortex after expansion. UV-vis extinction spectra (f) collected at the circled areas in (e) and average extinction spectrum over the whole image. For images taken through the eyepiece port, the black lines are the measuring graticules inside the eyepiece.

Biomedical Optics EXPRESS

stage. Better resolution will be obtained by using a high NA objective. The average 590 cm^{-1} peak SERS intensity emanating from stained structures and normalized to power and integration time was found to be about a factor of 2-3 lower than the average SERS intensity measured on similar stained structures before expansion, hence an estimated 50-60% loss in brightness which is similar to the estimated 50% loss in fluorescence signal reported in [6]. We also point out that the polyelectrolyte gel does not generate any measurable Raman signal and thus the maps only background signal originates from glass coverslip luminescence at 785 nm.

3.3. Plasmonic coupling effects in expansion microscopy with NPs labels

Enhanced optical absorption and Rayleigh scattering are achieved through the excitation of LSPR in noble metal nanoparticles [28, 29]. Significant efforts have been dedicated towards using LSPR properties in biosensing and imaging, with emphasis on their use as contrast agents in conventional optical imaging, photo-acoustic tomography, and dark-field imaging [30–36]. LSPR wavelengths in nanoparticles, as well as the magnitude and distribution of their resulting local electric field enhancement, depend on their material, size, shape, degree of aggregation, and the surrounding medium. LSPR occurs in the visible to NIR range for metals such as silver and gold. In the case of the proposed nanoparticles, LSPR is located at ≈540 nm (Section 2.1). Due to their small size (10 nm) and aspect ratio (1.3), it is expected from Mie theory that absorption is the main contribution to the high extinction cross-section per nanoparticle at the LSPR resonance and that the relative contribution of scattering is small. However, we could argue that such small nanoparticles can be loaded in much greater number per unit volume as compared to more efficient scatterers (for example 80 nm gold nanospheres) and thus provide sufficient scattering efficiency for a given volume to yield high contrast dark-field images before and after expansion.

After expansion, the dark-field images of the sample show an obvious color shift from gold/yellow (before expansion) to green (after expansion). To quantify this resonance shift, we recorded hyperspectral UV-visible extinction maps of regions of interest in dark-field illumination before and after expansion.

A dark-field microphotograph of NeuN labeling of the dentate gyrus before expansion (Fig. 4(a) shows gold/yellow structures over a darker background and the corresponding unprocessed total extinction intensity pixel by pixel shows a high signal-to-background ratio (Fig. 4(b)) where nanoparticles have accumulated, namely in the granule cells layer and some neuronal bodies in the pyramidal layer. Extinction spectra collected on these structures have broad linewidths with scattering wavelength spread over the 540-750 nm range and this trend is summarized on the average extinction spectrum over the whole area (insert). After tissue expansion, expanded neurons are bright green under dark-field illumination (Fig. 4(d) and 4(e)) and extinction spectra collected from different pixels on the stained structures show a much narrower spread in wavelength post-expansion with little deviation. The average spectrum of the whole map (insert) is remarkably narrow and similar to the extinction spectrum of the diluted NPs in Fig. 1, which indicates very little inhomogeneous broadening of the LSPR spectral width.

The change in optical response between the gold NPs staining before and after expansion can be understood as a consequence of the remarkable plasmonic properties of noble metal nanoparticles. The peak position and width of the collective LSPR response of an ensemble of nanoparticles is sensitive to electromagnetic coupling between them, mainly in the far field (dipole-dipole interaction) [37] and near field [34]. Near-field coupling in particular is relevant for particles in contact or in close proximity (≤5 nm). This phenomenon is now-well understood [38–40] and can be easily calculated for simple systems [41]. Strong near field coupling between two small (much smaller than wavelength) interacting metallic nanoparticles translates into a red-shift in the LSPR peak position whose magnitude decays exponentially with inter-particle distance. Figure 5(a) shows a dark-field close-up image of one of the concentric circular structures that a nanoparticle droplet has formed while fast drying on a glass substrate. The rings correspond

Biomedical Optics EXPRESS

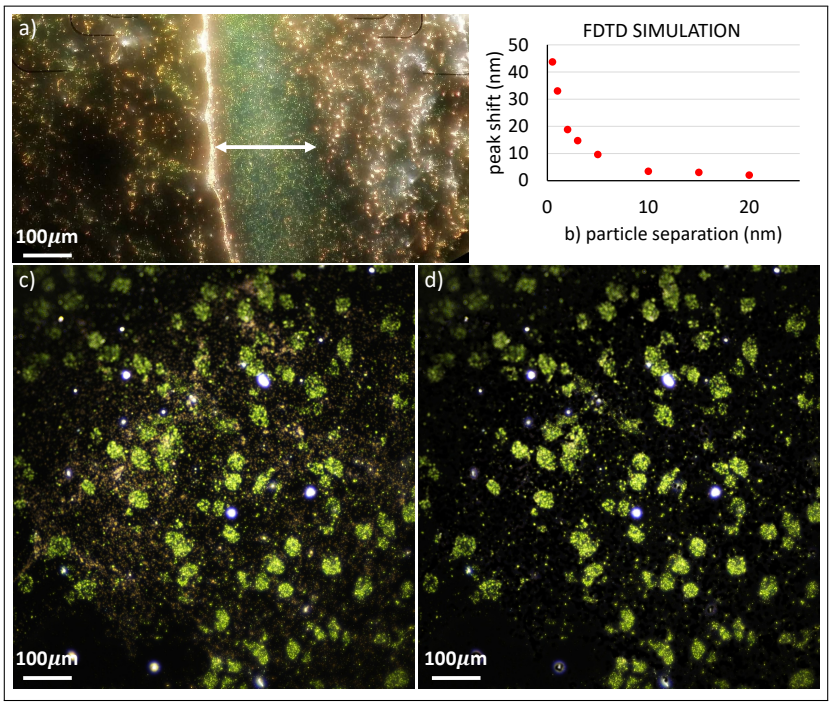

Fig. 5. Dark-field colorimetric discrimination of the aggregation state of the NPs labels. Dark-field detail (a) of a picture of the pure nanoparticles (1.2×10^{14} particles per mL) drop-dried on a glass slide. Note the visible color difference between aggregated and non-aggregated areas. Simulation results (b) for the extinction of two 10 nm gold nanospheres with spacing varying between 0.5 nm and 20 nm. Dark-field images of NeuN-NPs structures in expanded brain section before (c) and after (d) hue correction.

to progressive shrinkage of the drop with an alternation between yellow aggregates of NPs corresponding to the slow shrinking of the droplet and accumulation of nanoparticles along the rim and green dots valleys corresponding to sudden drop retraction while drying. Hence, when the NPs labels are sparse enough, the dominant green scattering is evident. Finite-difference time-domain (FDTD) simulation results for the near-field coupling effects for a dimer of 10 nm gold nanospheres on Fig. 5(b) illustrate this inter-particle distance-dependent phenomenon. The FDTD simulations were performed for two 10 nm gold nanoparticles placed in a uniform medium with refractive index of 1.33 (i.e. water). The mesh size was 1 nm and the simulation doamain was 2.5 μm×2.5 μm×2.5 μm [42]. Additionally, if we consider an assembly of nanoparticles, each particle is subject to the near-field of its neighbors, resulting in a much stronger coupling and hence a larger red-shift [39]. We hypothesize that, before expansion, the majority of the nanoparticles, bound to the NeuN epitopes, are in an aggregated state and strongly coupled to each other through near-field interaction which red-shifts the LSPR response from 540 nm up to 750 nm depending on both inter-particle distances and aggregate sizes. The subsequent treatment with AcX prepares the proteins, including the conjugated streptavidin of the labels, for anchorage to the gel. After digestion, using ExM with volume expansion in the 4X - 5X range, ensures that the labels that are properly incorporated into the gel matrix decouple. As a result, the dark-field scattering spectra of the expanded sections blue-shift towards the single, uncoupled extinction spectrum of isolated gold nanoparticles, which is narrowly distributed around 540 nm (green). Thus, when spatial information is taken into account through dark-field imaging or dark-field hyperspectral mapping, it is possible to infer the state of aggregation of the NPs pixel-by-pixel,

Biomedical Optics EXPRESS

which adds one other modality to the highly specific chemical signature these labels have through the enhanced Raman spectrum of their adsorbed dye.

One example illustrating this point is given in Fig. 5. An expanded mouse brain section stained for NeuN with the NPs labels and kept for 3 weeks in a moist environment at 4°C was imaged in dark-field conditions. Apart from the NeuN structures which appear bright green, many gold-colored aggregates can be seen in the background, most likely labels which detached from the gel matrix and aggregated. Using a simple threshold based on hue, only the green pixels which are corresponding to nanoparticles still bound to the expanded gel matrix are kept. The NPs which are specifically bound to the monoclonal NeuN primariy-biotin secondary structures should have a much larger density than the sparse unspecifically-bound NPs which were successfully anchored to the gel, resulting in very high contrast corrected dark-field images of NeuN distribution in expanded brain sections.

Earlier we observed an average SERS intensity reduction of approximately 2-3 fold. While this has been expected because of the dilution effect after expansion, its magnitude is worth additional considerations. In particular, the SERS intensity decrease does not appear to scale linearly with the expansion factor. For example, a 4X linear expansion will dilute 2-D imaging intensity by roughly 16X. Here we provide two possible explanations for the observed intensity reduction. First, when the tissue is expanded, the originally clustered NPs properly attached to the gel matrix become farther away, causing decoupling and color change. However, the overall expanded cluster might still reside within a single diffraction limited pixel, and their SERS intensities are still summed together. Another possible source of non-linearity is the strong optical attenuation of NPs. Before expansion, the crowdedness of NPs causes more round-trip attenuation (laser excitation and SERS return signal) than that for the post-expansion sample. To further understand the SERS intensity quantitatively, a systematic study of the modification of the SERS enhancement distribution upon expansion of the tissue is currently underway. We finally note that the gold nanoparticles did not penetrate the entire mouse brain section within the incubation time we used (1 hour). In addition, the significant larger size of the NPs compare to fluorophores could have reduced the diffusion of NPs inside the tissue. To improve the accessibility of antigens, surfactants would be a potential facilitator.

4. Conclusion

In this study, we demonstrate the feasibility of using plasmonic nanoparticle-based expansion microscopy with both SERS and dark-field spectroscopic imaging. This technique provides several advantages over conventional fluorescence labeling. The SERS signal brightness and the absence of background allow for short imaging times, and there is no degradation of the signal intensity over time and under high power illumination. The dark-field scattering continues to be visible throughout the expansion process, and the significant color change is indicative of tissue expansion. The color change has been further examined by dark-field spectroscopy, which reveals the uncoupling of nanoparticles after expansion. Although only one SERS active nanotag has been demonstrated here, the results establish the feasibility of nanoparticle-based expansion microscopy. Given the significant body of work demonstrating the multiplexing capabilities of SERS labeling [9, 43–45], further extension of this work to more NPs tags is currently in progress [46].

Funding

National Science Foundation (NSF) grants NSF-1151154 and NSF-1605683, the I/UCRC BRAIN Center CNS-1650536, the National Institutes of Health (NIH) #4 R00 LM011390-02, and the Cancer Prevention and Research Institute of Texas (CPRIT) #RR140013.

Biomedical Optics EXPRESS

Acknowledgments

The authors would like to thank Jingting Li for her training and assistance with the line-scan Raman imaging system. We would also like to thank Chris Schoen and Nanopartz for their assistance in tuning NP size and shape to optimize optical properties and binding.

Disclosures

The authors declare that there are no conflicts of interest related to this article.